

Cite this: *J. Mater. Chem. C*, 2022, 10, 4128Received 25th December 2021,  
Accepted 21st February 2022

DOI: 10.1039/d1tc06106b

rsc.li/materials-c

# Hot hole transfer from Ag nanoparticles to multiferroic $\text{YMn}_2\text{O}_5$ nanowires enables superior photocatalytic activity†

Kazi M. Alam,<sup>\*ab</sup> Sergey Gusarov,<sup>\*b</sup> Mustafa Supur,<sup>id c</sup> Pawan Kumar,<sup>a</sup>  
Alexander E. Kobryn,<sup>b</sup> Kai Cui,<sup>b</sup> Richard L. McCreery,<sup>id c</sup> and Karthik Shankar<sup>id \*a</sup>

Plasmonic hot carriers with a nonthermal distribution of kinetic energies have opened up new avenues in photovoltaics, photodetection and photocatalysis. While several articles have reported ultrafast hot electron injection from coinage metals into n-type semiconductors across Schottky barriers and efficient subsequent utilization of injected hot electrons, reports of hot hole harvesting are comparatively rare due to the difficulty in forming Schottky junctions between p-type semiconductors and high work function metals. In this work, we report the fabrication, characterization and theoretical calculations of a novel integrated multiferroic-plasmonic system comprising  $\text{YMn}_2\text{O}_5$  nanowires decorated on their surface with Ag nanoparticles (NPs). A Schottky barrier for holes exists at the  $\text{YMn}_2\text{O}_5$ -Ag hetero-interface and hot holes are injected from Ag across this barrier. The synthesized hybrid along with bare Ag NPs were tested for Raman surface photocatalytic reduction of 4-NBT (4-nitrobenzenethiol) to DMAB (*p,p'*-dimercaptoazobenzene) where the composite demonstrated superior activity compared to the bare metal. Ultraviolet photoelectron spectroscopy (UPS) revealed a significantly reduced work function of the composite compared to the pristine Ag, indicative of more energetic hot electrons on the surface of the composite required for efficient photoreduction. Density functional theory (DFT)-based calculations revealed localization of molecular orbitals supportive of a possible hole transfer from  $\text{YMn}_2\text{O}_5$  to Ag and a reorganization of electronic states, which promotes increased phonon-mediated sp-intraband damping of the plasmon. DFT results also indicated a purely electronic contribution to the ferroelectric polarization of  $\text{YMn}_2\text{O}_5$  over and above the ionic contribution, which originated from the magnetic polarization of O2p states.

## 1. Introduction

Multiferroics belong to a fundamentally distinct class of materials within the condensed matter family, where two or more ferroic orders simultaneously exist.<sup>1</sup> In general, these two ferroic orders refer to magnetism and ferroelectricity, which are two chemically contraindicated or mutually exclusive phenomena.<sup>2,3</sup> These systems hold great potential for multifunctional devices, primarily due to the tunability of their electronic and magnetic properties by external magnetic and electric fields, respectively, as a consequence of complex coupling between the two ferroic orders.<sup>2-5</sup> While the majority of current state-of-the-art research studies are devoted to unravelling the fundamental science, these materials have found some intriguing technological applications mostly in the microelectronics area, such as memory and logic devices.<sup>1,6,7</sup> The highly unusual physical properties and combination of chemistry needed for achieving multiferroicity in these systems are also beneficial in other areas such as biomedical engineering, photovoltaics, photocatalysis, cosmology and high energy physics.<sup>7</sup> To date, bismuth ferrite ( $\text{BiFeO}_3$ ) is arguably the most studied multiferroic material in the current literature, primarily due to its highest ferroelectric polarization and room temperature multiferroic properties.<sup>1,8-10</sup> It is also the most sought after multiferroic material to explore photocatalytic applications.<sup>7,11</sup>  $\text{BiFeO}_3$  belongs to type-I multiferroics as the ferroelectricity is independent of magnetic ordering.<sup>12</sup> On the other hand, type-II materials, where ferroelectricity emerges due to some specific magnetic orders such as perovskite oxide  $\text{YMn}_2\text{O}_5$ , have rarely been explored in catalytic applications.<sup>12-15</sup>

<sup>a</sup> Department of Electrical and Computer Engineering, University of Alberta, Edmonton, AB T6G 1H9, Canada. E-mail: kmalam@ualberta.ca, kshankar@ualberta.ca; Tel: +1780-492-1354

<sup>b</sup> Nanotechnology Research Centre, National Research Council Canada, 11421 Saskatchewan Drive, Edmonton, AB T6G 2M9, Canada. E-mail: gusarov@ualberta.ca

<sup>c</sup> Department of Chemistry, University of Alberta, Edmonton, Alberta T6G 2G2, Canada

† Electronic supplementary information (ESI) available. See DOI: 10.1039/d1tc06106b

Coupling plasmonic metals with semiconductors offers a viable route to realize enhanced activity in photovoltaics, photodetectors and photocatalysts due to synergistic effects.<sup>16–18</sup> When the semiconductor is a ferroelectric material, some additional advantageous features can be achieved. Surface ferroelectric polarization can be tuned to manipulate the interfacial barrier heights in order to facilitate efficient charge separation and extend the hot electron lifetime, thus, adding an extra degree of freedom to realize tunable systems for solar energy harvesting applications.<sup>10,19–24</sup> Coupling ferroelectric materials with plasmonic metals offers many other opportunities, such as, realization of 2D plasmonic arrays through the exploitation of ferroelectric domain walls,<sup>25</sup> hybrid ferroelectric-plasmonic waveguides for all-optical logic gates,<sup>26</sup> and plasmon-assisted solid state nanolasers and nonlinear radiation sources.<sup>27</sup> Enhanced ferromagnetism and spin-dependent transport in Ag coupled multiferroic  $\text{Bi}_2\text{Fe}_4\text{O}_9$  was identified for improved electrocatalytic performance compared to pristine  $\text{Bi}_2\text{Fe}_4\text{O}_9$ .<sup>28</sup> A synergistic effect of localized surface plasmonic resonance (LSPR) of Au particles and ferroelectric polarization of  $\text{BiFeO}_3$  resulted in enhanced photoelectrochemical water splitting.<sup>29</sup> A plasmonic multiferroic system comprising Ag nanoparticle decorated  $\text{BiFeO}_3$  is reported to outperform the pristine multiferroic in photocatalytic activity.<sup>30</sup> Integrating multiferroics with plasmonic metals is attempted for other applications as well. For example, the  $\text{LuFe}_2\text{O}_4$  multiferroic has been used as a substrate to tune the plasmonic response of Au nanoparticles to achieve tunability of surface-enhanced-Raman scattering (SERS), primarily through modulation of the substrate's dielectric properties.<sup>31</sup> A theoretical study of metal-multiferroic systems revealed that a variation of the effective dielectric response of the metal resulted from magnetoelectric interaction.<sup>32</sup> However, from the perspective of solar energy harvesting, the current knowledge of plasmon-induced hot carrier dynamics at the ferroelectric-plasmonic interfaces still remains in its infancy, while multiferroic-plasmonic systems are even more rare. In this study, we have studied the interactions between multiferroic  $\text{YMn}_2\text{O}_5$  nanowires and plasmonic Ag nanoparticles (NPs) through a combination of Stokes anti-Stokes Raman thermometry, Raman surface catalytic reduction of 4-NBT to DMAB and ultraviolet photoemission spectroscopy (UPS), which agrees well with DFT-based calculations.

The harvesting of hot holes in such plasmon-semiconductor heterojunctions is relatively rare<sup>33–35</sup> in comparison to the large number of reports on successful hot electron harvesting in junctions between n-type semiconductors and coinage metals. One major engineering problem is the difficulty in achieving high performance Schottky barriers between p-type semiconductors and high work function coinage metals. In this study, we demonstrate a potential barrier for holes at the  $\text{YMn}_2\text{O}_5$ -Ag interface.

## 2. Results and discussion

### 2.1 Physicochemical characterization of $\text{YMn}_2\text{O}_5$ -Ag nanocomposites

The hydrothermal route was employed to synthesize the  $\text{YMn}_2\text{O}_5$  nanowires using yttrium nitrate hexahydrate as the

Y precursor and manganese acetate tetrahydrate and potassium permanganate as the Mn precursors. The details of the synthesis steps can be found in the ESI.† The morphology and fine structural features were analyzed by transmission electron microscopy (TEM). Fig. 1a shows the TEM image of mullite  $\text{YMn}_2\text{O}_5$  nanowire bundles, while Fig. 1b and c show the high-resolution TEM images of bare  $\text{YMn}_2\text{O}_5$  and  $\text{YMn}_2\text{O}_5$ -Ag hybrid nanowires, respectively. The average diameter and length of these hydrothermally grown nanowires are  $\sim 7$  and 150 nm, respectively. It is worth mentioning that one recent study reported the growth of rod-like  $\text{YMn}_2\text{O}_5$  nanostructures having a larger average diameter (50–70 nm) using a similar hydrothermal route.<sup>36</sup> Unlike our synthesis protocol, they have used manganese chloride tetrahydrate as the Mn precursor. The hydrothermal process has also been pursued by a few other research groups in the past, which all reported the synthesis of much larger particles.<sup>37,38</sup> Selected regions of Fig. 1c are shown in Fig. 1d–g, which revealed the lattice planes of orthorhombic  $\text{YMn}_2\text{O}_5$  and face-centered-cubic Ag discussed later. Fig. 1h shows a bundle of hybrid nanowires and Fig. 1i–l show the elemental mappings of the constituent elements. The chemical valence states and surface chemical compositions of the materials were investigated by X-ray photoelectron spectroscopy (XPS). The XPS survey scans of pristine  $\text{YMn}_2\text{O}_5$  and  $\text{YMn}_2\text{O}_5$ -Ag nanowires displayed all the core level (Y3d, Mn2p, O1s and Ag3d) and sub-core-level (OKLL, MnLLM, Y3p, Y3s, Y4p, Y4s, and O2s) peaks confirming the presence of all the constituent elements (Fig. 2a). The deconvoluted core-level high-resolution XPS (HR-XPS) spectra of pristine  $\text{YMn}_2\text{O}_5$  nanowires in the Y3d region show two well-resolved peaks at 156.9 and 158.9 eV assigned to  $\text{Y}3\text{d}_{5/2}$  and  $\text{Y}3\text{d}_{3/2}$  peak components of Y present in the 2+ oxidation state (Fig. 2b and f).<sup>39</sup> The  $\text{YMn}_2\text{O}_5$ -Ag samples also displayed two peaks in the Y3d region at binding energy (BE) values of 157.3 and 159.3 eV. In contrast to the pristine sample, the peak separation was less prominent in the composite sample, which might be a consequence of the coverage of the  $\text{YMn}_2\text{O}_5$  surface with Ag, resulting in interruption of the signal gains of Y3d. The HR-XPS spectra of both the samples in the Mn2p region were composed of two well-separated peaks that originated from  $\text{Mn}2\text{p}_{3/2}$  and  $\text{Mn}2\text{p}_{1/2}$  peak components (Fig. 2c and g). Two deconvoluted peaks of  $\text{Mn}2\text{p}_{3/2}$  located at 641.5 and 643.4 eV along with  $\text{Mn}2\text{p}_{1/2}$  peaks at 652.6 and 655.3 eV were assigned to Mn present in 3+ and 4+ oxidation states.<sup>13,37</sup> The separation between  $\text{Mn}^{3+}$  and  $\text{Mn}^{4+}$  peak components was found to be 1.9 eV suggesting the presence of Mn in the mullite system. The  $\text{Mn}^{3+}/\text{Mn}^{4+}$  ratio values for pristine  $\text{YMn}_2\text{O}_5$  nanowires and  $\text{YMn}_2\text{O}_5$ -Ag samples were calculated by integration of the peak areas and were found to be 2.33/1 and 2.22/1, respectively, demonstrating deviation from the ideal ratio of 1:1 in the mullite phases. This suggests the presence of plenty of oxygen vacancies in the samples, which are beneficial for hole conduction and oxidation reactions.<sup>14</sup> It should be noted that the deconvolution of  $\text{Mn}2\text{p}_{3/2}$  and  $\text{Mn}2\text{p}_{1/2}$  peaks can result in multiple fits with different  $\text{Mn}^{3+}$  and  $\text{Mn}^{4+}$  ratios. Thus, we opted to rely on software (CasaXPS) to determine the best combination of these peaks giving rise to the envelope

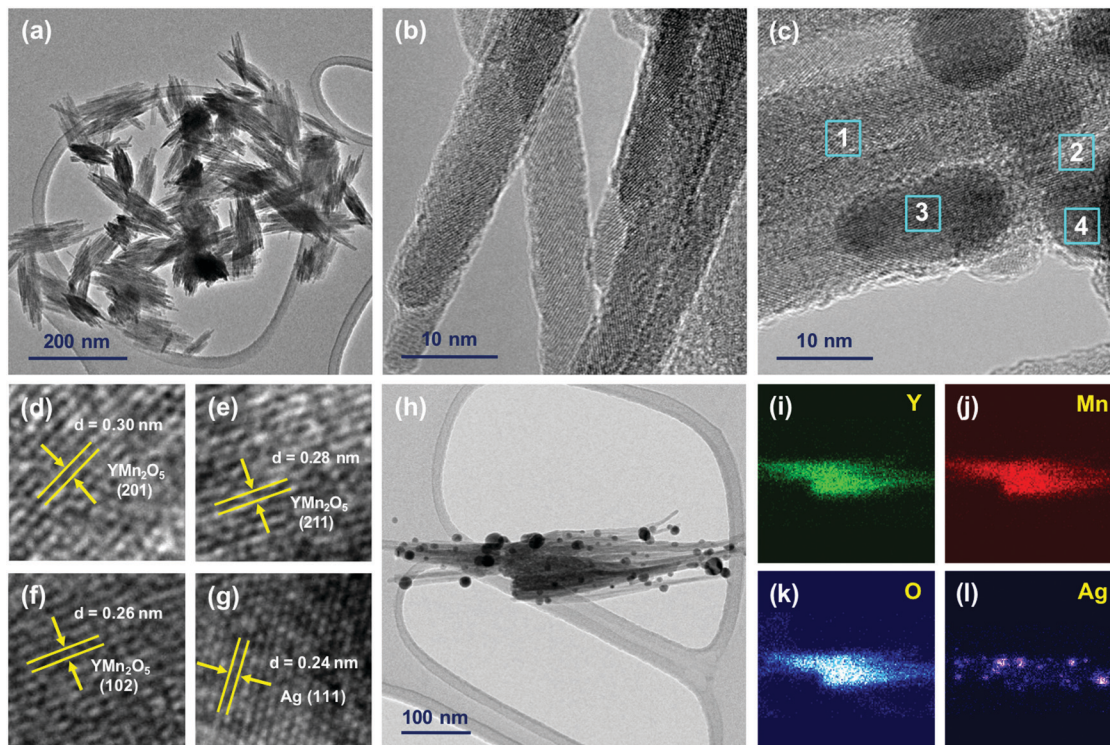


**Fig. 1** (a) Low-resolution TEM image showing the pristine  $\text{YMn}_2\text{O}_5$  nanowires in a bundled form. High-resolution TEM images of (b) pristine  $\text{YMn}_2\text{O}_5$  nanowires and (c)  $\text{YMn}_2\text{O}_5$ -Ag hybrid nanowires showing spherical Ag nanoparticles attached to  $\text{YMn}_2\text{O}_5$  nanowires. (d-g) Selected magnified regions, showing different lattice planes of  $\text{YMn}_2\text{O}_5$  and face-centered cubic Ag for regions corresponding to the (1)-(4) marked regions of (c), respectively. (h) Scanning TEM (STEM) image of a bundle of  $\text{YMn}_2\text{O}_5$ -Ag hybrid nanowires. STEM elemental mappings for (i) Y, (j) Mn, (k) O and (l) Ag.

function that fits the experimentally generated data points. Two peak components in O1s HR-XPS of the pristine  $\text{YMn}_2\text{O}_5$  and  $\text{YMn}_2\text{O}_5$ -Ag sample at BE  $\approx$  529.3 and 531.2 eV were attributed to lattice oxygens ( $\text{O}_{\text{latt}}$ ) of  $\text{YMn}_2\text{O}_5$  and non-lattice surface adsorbed adventitious oxygens ( $\text{O}1\text{s}_{(\text{non.latt.})}/\text{-OH}$ ), respectively (Fig. 2d and h).<sup>14</sup> The peaks at 368.0 and 374.0 eV in the Ag3d region of the  $\text{YMn}_2\text{O}_5$ -Ag sample originated from  $\text{Ag}3\text{d}_{5/2}$  and  $\text{Ag}3\text{d}_{3/2}$  peak components of Ag present in the zerovalent metallic state (Fig. 2e).<sup>40</sup>

Electron energy loss spectroscopy (EELS) spectra of pristine  $\text{YMn}_2\text{O}_5$  and  $\text{YMn}_2\text{O}_5$ -Ag hybrid for the O-K and Mn-L edges are shown in Fig. 3a.<sup>41-43</sup> A shift towards higher energy loss in the composite for all these edges was observed with respect to those of pristine  $\text{YMn}_2\text{O}_5$ , which implies strong interaction between them. UV-Vis absorption spectra collected in diffuse reflectance mode (Fig. 3b) also showed this strong interaction as evidenced by enhanced absorption of the composite in the entire visible spectrum.<sup>15,36</sup> However, the LSPR peak of Ag (inset of Fig. 3b) was not identifiable due to an overlap with one absorption peak of bare  $\text{YMn}_2\text{O}_5$ . The X-ray diffraction (XRD) pattern of pristine  $\text{YMn}_2\text{O}_5$  is shown in Fig. 3c, which confirms the orthorhombic phase of  $\text{YMn}_2\text{O}_5$  (JCPDS Card No. 34-0667).<sup>13,15</sup> The XRD pattern of the  $\text{YMn}_2\text{O}_5$ -Ag/ $\text{YMn}_2\text{O}_5$ -Ag composite reproduced all these peaks with additional Ag peaks in the fcc phase.<sup>44</sup> Fig. 3d and e show the Stokes and anti-Stokes Raman spectra of pristine  $\text{YMn}_2\text{O}_5$  and the  $\text{YMn}_2\text{O}_5$ -Ag hybrid, respectively. The vibrational modes at  $628\text{ cm}^{-1}$  and

$702\text{ cm}^{-1}$  can be attributed to  $A_g$  symmetry that involves stretching vibrations of oxygen atoms of Mn-O polyhedra.<sup>4</sup> While the Stokes Raman signal strength is proportional to the rate of transition of a molecule from ground state to the first vibrational state, the anti-Stokes signal intensity is a manifestation of the reverse transition rate.<sup>45</sup> In these Stokes and anti-Stokes Raman thermometry experiments, a charge-coupled device (CCD) detector was used, which works on the photon counting principle. The lattice temperatures of the pristine  $\text{YMn}_2\text{O}_5$  and  $\text{YMn}_2\text{O}_5$ -Ag composite were calculated according to the following equation that is derived from the Boltzmann population distribution of the ground and the first excited states.<sup>46</sup>

$$\frac{I_{\text{AS}}}{I_{\text{S}}} = \frac{(V_1 + V_v)^3}{(V_1 - V_v)^3} \exp\left(\frac{-hV_v}{kT}\right) \quad (1)$$

In the above expression,  $I_{\text{AS}}$  and  $I_{\text{S}}$  are the Stokes and anti-Stokes Raman signal intensities, respectively,  $V_1$  and  $V_v$  are the frequencies of the Raman laser and the specific Raman vibrational mode of the probed material, respectively,  $k$  is the Boltzmann constant,  $h$  is the Planck's constant and  $T$  is the absolute temperature of the probed material. The lattice temperature was determined using the vibrational modes at  $628\text{ cm}^{-1}$  and  $702\text{ cm}^{-1}$ . The calculated average lattice temperatures of pristine  $\text{YMn}_2\text{O}_5$  and  $\text{YMn}_2\text{O}_5$ -Ag hybrid were

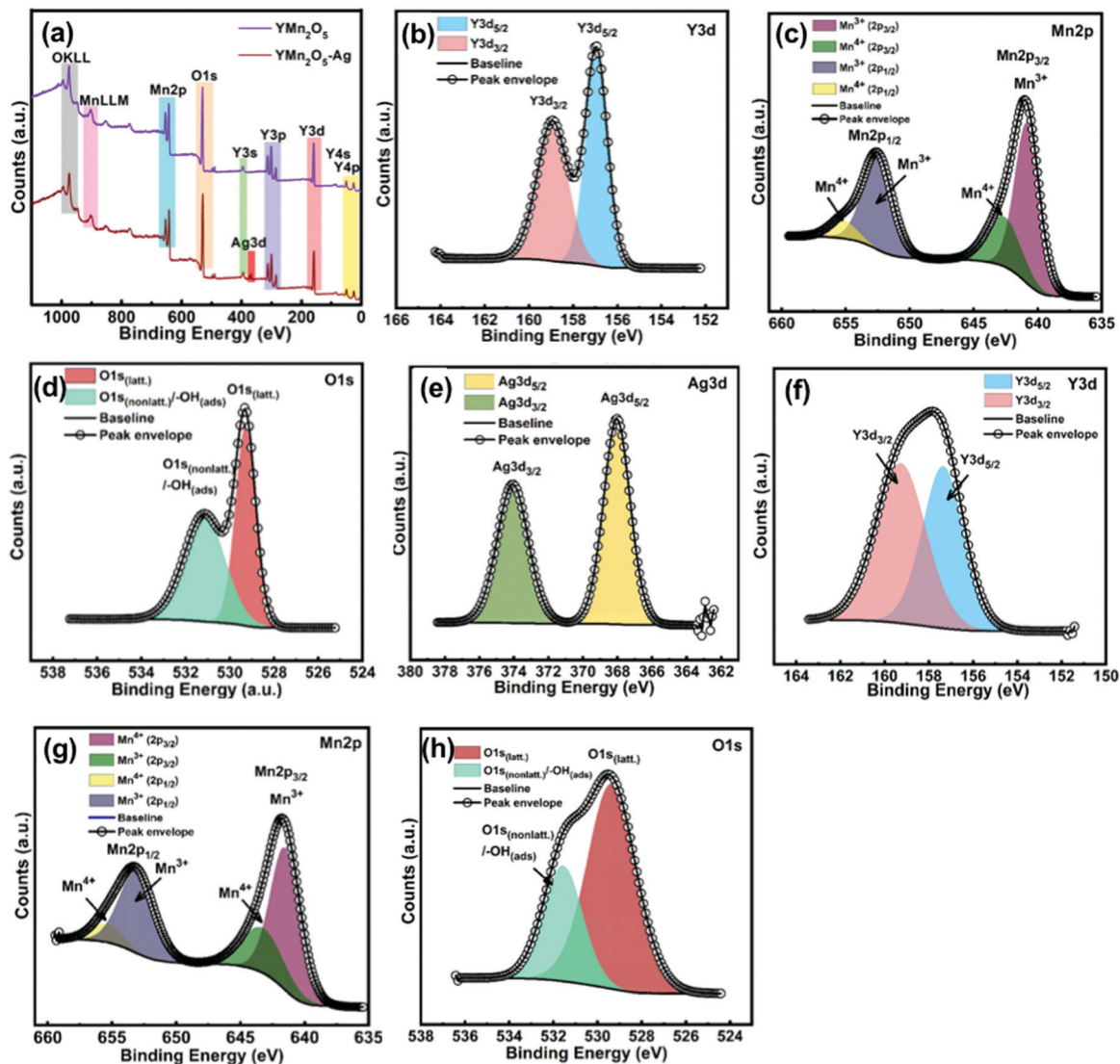


Fig. 2 (a) XPS elemental survey scans of pristine  $\text{YMn}_2\text{O}_5$  and  $\text{YMn}_2\text{O}_5\text{-Ag}$  hybrid. High resolution XPS spectra of pristine  $\text{YMn}_2\text{O}_5$  in the (b) Y3d region, (c) Mn2p region and (d) O1s region. High resolution XPS spectra of the  $\text{YMn}_2\text{O}_5\text{-Ag}$  hybrid in the (e) Ag3d region, (f) Y3d region, (g) Mn2p region and (h) O1s region.

$\sim 338$  K and 355 K, respectively. Localized surface plasmons in coinage metals can undergo damping either radiatively or nonradiatively, where the latter plasmon relaxation route results in the generation of energetic hot carriers.<sup>47–49</sup> Plasmon induced hot carrier injection from the metal to the coupled adsorbate system can be probed by monitoring the enhanced anti-Stokes scattering rate in comparison to the thermodynamically equilibrated system.<sup>50</sup> The slight rise of temperature in the hybrid, compared to bare  $\text{YMn}_2\text{O}_5$  indicates significant backscattering of plasmonic hot electrons from  $\text{YMn}_2\text{O}_5$  to Ag, possibly as a result of the absence of a barrier that can keep them confined in  $\text{YMn}_2\text{O}_5$ . This observation is typical for the coupled plasmonic metal-excitonic system comprising a semiconductor that has a higher work function than the attached metal, which results in downward band-bending at the metal–semiconductor interface.<sup>19,51</sup> Ultraviolet

photoelectron spectroscopic results, discussed later in this report, confirmed this downward band bending. Carrier back-scattering is a much faster process than thermal cooling. Thus, we surmise that the observed temperature rise of 40–50 °C over room temperature might be a result of some hot hole (but not hot electron) injection from Ag into adjacent  $\text{YMn}_2\text{O}_5$ . More details of the possible mechanism are discussed later in this report.

Raman surface photocatalytic reduction of 4-NBT (4-nitrobenzenethiol) to DMAB (*p,p'*-dimercaptoazobenzene) was conducted on the bare Ag and  $\text{YMn}_2\text{O}_5\text{-Ag}$  hybrid. Fig. 4a shows the Raman spectra of 4-NBT and DMAB (bottom and top panels, respectively), while Fig. 4b shows the chemical structures of 4-NBT and DMAB. The Raman peaks at 1101, 1332 and 1576  $\text{cm}^{-1}$  of 4-NBT are assigned to S–C stretching vibration,  $\text{NO}_2$  vibration and C=C stretching vibration of the benzyl ring,

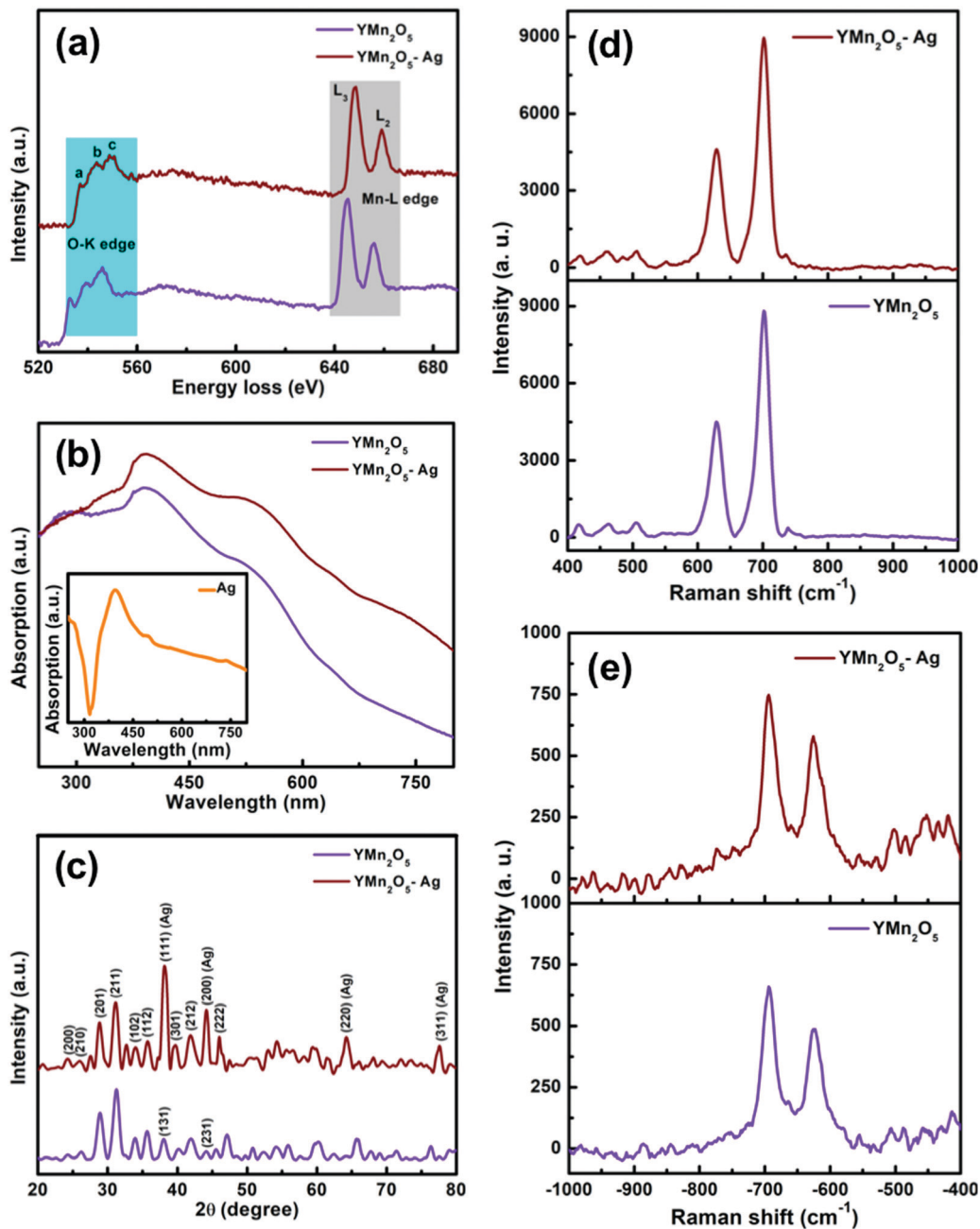


Fig. 3 (a) EELS spectra for O–K and Mn–L edges of the pristine  $\text{YMn}_2\text{O}_5$  and  $\text{YMn}_2\text{O}_5\text{-Ag}$  hybrid. (b) Diffuse reflectance absorption spectra of the pristine  $\text{YMn}_2\text{O}_5$  and  $\text{YMn}_2\text{O}_5\text{-Ag}$  hybrid; the inset shows the spectrum for the bare Ag nanoparticles on a glass substrate. (c) XRD plots of pristine  $\text{YMn}_2\text{O}_5$  and  $\text{YMn}_2\text{O}_5\text{-Ag}$  hybrid; the EELS and XRD plots are vertically separated for better visibility. (d) Stokes and (e) anti-Stokes Raman spectra of the pristine  $\text{YMn}_2\text{O}_5$  and  $\text{YMn}_2\text{O}_5\text{-Ag}$  hybrid.

respectively.<sup>52,53</sup> DMAB Raman peaks are identified at 1142, 1392 and 1439  $\text{cm}^{-1}$ . The band at 1142  $\text{cm}^{-1}$  is attributed to C–N stretching vibration, and the N=N stretching-related peaks at 1392 and 1439  $\text{cm}^{-1}$  arise due to  $\text{ag}_{16}$  and  $\text{ag}_{17}$  vibrational modes of DMAB, respectively.<sup>52,54</sup> Fig. 4a shows the comparative catalytic efficiencies at a constant laser power of 1 mW, while Fig. 4c and d show the gradual increase of the product peaks with a simultaneous reduction of reactant peaks

as a function of laser power. It is extraordinary that the product-specific peaks of DMAB at 1142, 1392 and 1439  $\text{cm}^{-1}$  are strongly evident in the Raman spectrum of the  $\text{YMn}_2\text{O}_5\text{-Ag}$  hybrid even at a low laser power of 0.1 mW, while contrastingly, these same DMAB peaks are quite weak in the Raman spectrum of pristine Ag at 0.1 mW laser power, unambiguously indicating the dramatically enhanced photocatalytic ability of the hybrid. The Raman peak intensity ratios ( $I_{\text{NBT}}/I_{\text{DMAB}}$ ) of the reactant

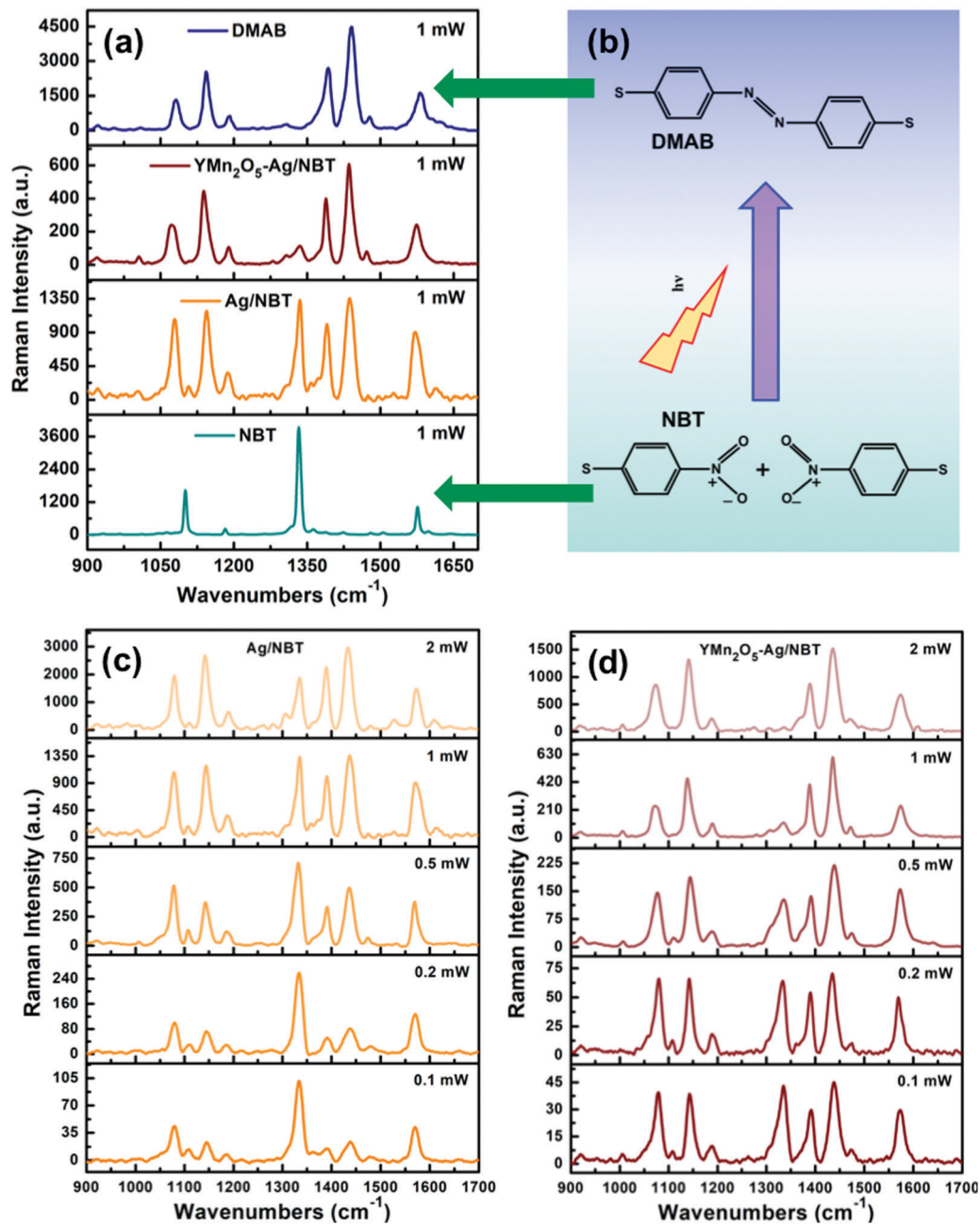


Fig. 4 Surface catalytic conversion of 4-NBT (nitrobenzenethiol) to DMAB (*p,p'*-dimercaptoazobenzene) monitored by Raman spectroscopy. (a) Comparative performance of surface catalytic conversion of 4-NBT to DMAB at 1 mW laser power; from the top, Raman spectra of pristine DMAB, 4-NBT on the YMn<sub>2</sub>O<sub>5</sub>-Ag hybrid, 4-NBT on pristine Ag, and pristine 4-NBT. (b) Chemical structures of 4-NBT and DMAB. Laser power-dependent spectral evolution of the reactant (4-NBT) and product (DMAB) for (c) 4-NBT on pristine Ag and (d) 4-NBT on the YMn<sub>2</sub>O<sub>5</sub>-Ag hybrid.

(4-NBT) and product (DMAB) on pristine Ag and on the YMn<sub>2</sub>O<sub>5</sub>-Ag hybrid as a function of laser power have been calculated from Fig. 4c and d and plotted (Fig. S1 in the ESI<sup>†</sup>).  $I_{\text{NBT}}$  was estimated from the 4-NBT peak at  $\sim 1332 \text{ cm}^{-1}$  and  $I_{\text{DMAB}}$  was estimated from the DMAB peak at  $\sim 1439 \text{ cm}^{-1}$ . Clearly, at any laser power the  $I_{\text{NBT}}/I_{\text{DMAB}}$  value is much lower in the case of the YMn<sub>2</sub>O<sub>5</sub>-Ag hybrid compared to pristine Ag, which indicates superior catalytic performance of the former due to the 4-NBT to DMAB reaction proceeding to completion. Surface plasmon relaxation-induced energetic hot

electrons in plasmonic Ag are injected into 4-NBT to perform this reduction.<sup>52,55</sup>

Fig. 4 clearly shows the superior catalytic activity of the hybrid compared to pristine Ag, which we attribute to the superior hot carrier pair separation in the YMn<sub>2</sub>O<sub>5</sub>-Ag hybrid due to hot hole injection from Ag into YMn<sub>2</sub>O<sub>5</sub> enabling the more efficient reduction of 4-NBT by hot electrons in Ag. The possible routes of this reaction in both stand-alone Ag and its composite with YMn<sub>2</sub>O<sub>5</sub> are discussed in detail later in this report.

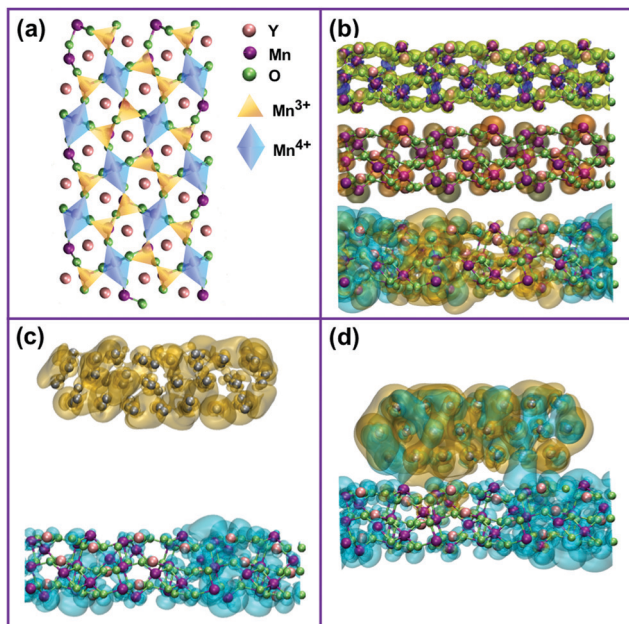


Fig. 5 (a) Atomic arrangement of  $\text{YMn}_2\text{O}_5$  showing pyramidal and octahedral Mn atoms. (b) Side views showing different isosurfaces of DFT optimized pristine  $\text{YMn}_2\text{O}_5(201)$ ; from the top, electron density difference where the transparent blue and yellow surfaces represent charge depletion and accumulation regions, respectively (the isosurface value is set to  $0.012 \text{ eV \AA}^{-3}$ ), spin density difference where the transparent olive and orange surfaces represent spin-up and spin-down electron dominated regions, respectively (the isosurface value is set to  $0.03 \text{ eV \AA}^{-3}$ ) and spatial distributions of molecular orbitals where the transparent cyan and gold surfaces represent HOMO and LUMO, respectively; the HOMO and LUMO surfaces of  $\text{YMn}_2\text{O}_5(201)$ -Ag heterosystems for the (c) far configuration and (d) close configuration. Pink, purple, lime and silver colours are for Y, Mn, O and Ag atoms, respectively.

## 2.2 Density functional theory computations

Density functional theory (DFT) based quantum chemical calculations were employed to extract and analyze the electronic properties of the pristine  $\text{YMn}_2\text{O}_5$  and  $\text{YMn}_2\text{O}_5$ -Ag composite systems. The details for the construction of the structures prior to computation and modeling parameters have been described in the ESI.† Fig. 5a shows the atomic arrangement of perovskite  $\text{YMn}_2\text{O}_5$  with an octahedrally coordinated Mn atom ( $\text{Mn}^{4+}$ ) and pyramidally coordinated Mn atom ( $\text{Mn}^{3+}$ ). Fig. 5b and Fig. S2 in the ESI† show electron density difference isosurfaces of bare  $\text{YMn}_2\text{O}_5(201)$  where charge depletion and accumulation regions are found in accordance with the constituent atoms' electronegativity order. Spin density isosurfaces that graphically represent the differences between the densities of up-spin and down-spin electrons<sup>56</sup> are visible in these figures, consistent with the paramagnetic nature of the Mn atoms. Fig. 5b and Fig. S2 in the ESI† also show the highest occupied molecular orbital (HOMO) and the lowest unoccupied molecular orbital (LUMO) of bare  $\text{YMn}_2\text{O}_5(201)$ , which are spatially separated. Fig. 5c and d show the molecular orbital positions for  $\text{YMn}_2\text{O}_5(201)$  and Ag(111) systems in distant (far) and proximal (close) configurations, respectively. These figures reveal the clear HOMO and LUMO localization on  $\text{YMn}_2\text{O}_5$  and Ag,

respectively, for both cases. Such a spatial distribution of frontier orbitals predicts the photoexcited charge carrier transport direction from  $\text{YMn}_2\text{O}_5$  to Ag in the hybrids as follows – lower energy states for holes exist in  $\text{YMn}_2\text{O}_5$ , while lower energy states for electrons exist in Ag.

The total wave function is projected onto the orthogonalized atomic wave functions to obtain the projected energy density of states (PDOS). Fig. S3 in the ESI† and Fig. 6 show the PDOS of selected Y, Mn and O atoms of pristine  $\text{YMn}_2\text{O}_5$  (201) and the corresponding orbital-resolved PDOS. PDOS of selected Y, Mn and O atoms of DFT optimized  $\text{YMn}_2\text{O}_5(201)$ -Ag heterosystems in the far and close configurations are shown in Fig. 7a and b. As expected, the spin-up Mn atom shows more up-spin states than down-spin states while the spin-down Mn atom shows more down-spin states than up-spin states. This is specifically manifested in the occupied region. According to these figures, nonmagnetic O2p states are not perfectly spin-symmetric. Such spin-dependent asymmetry in the O2p states originates from the nature of covalency between the Mn and O atoms in  $\text{YMn}_2\text{O}_5$ . Multiferroicity or magnetically driven ferroelectricity emerges from the spin-dependent Mn-O hybridization.<sup>57</sup> Resonant soft X-ray scattering results at the O-K edge and DFT calculations revealed this magnetic polarization of the O2p states as a consequence of strong spin-dependent hybridization of O2p and Mn3d states, resulting in a purely electronic contribution to the ferroelectric polarization.<sup>57–59</sup> Therefore, in addition to the ionic contribution, ferroelectric polarization in  $\text{YMn}_2\text{O}_5$  has an electronic contribution.<sup>58</sup> Orbital-resolved PDOS spectra of Ag atoms in the far and close configurations are shown in Fig. 7c and d, respectively. Compared to those in the far configuration, in the close geometry, the occupied and unoccupied states of Ag are more localized in the immediate vicinity of the Fermi level with enhanced intensity. Such strong interaction-induced electronic reorganization of plasmonic metal states is suggestive of an increased phonon-mediated sp-intraband transition probability under illumination conditions, necessary for energetic hot electron generation. It is worth mentioning that in Ag, this sp-intraband transition is the dominant mechanism of ultrafast Landau damping-mediated hot carrier generation.<sup>60,61</sup> Note that the size of the Ag cluster of atoms in these DFT calculations is much smaller than the actual particle size revealed by TEM discussed earlier. Thus, the sp-intraband transition is expected to have a geometry-assisted contribution apart from the phonon-assisted route.<sup>62</sup> Nevertheless, the strong-interaction induced reorganization of electronic states in the close configuration of the  $\text{YMn}_2\text{O}_5$ -Ag system is what stands out in this analysis, as the additional geometry-assisted intraband contribution is present in both the far and close configurations, where the size of the Ag clusters remains the same.

## 2.3 Band alignment at the $\text{YMn}_2\text{O}_5$ -Ag hetero-interface

Ultraviolet photoelectron spectroscopy (UPS) was used to determine the work function ( $\phi$ ) of the materials. The details of the work function calculation method can be found in the ESI.† Work function values of 4.38, 4.15 and 3.11 eV were found for

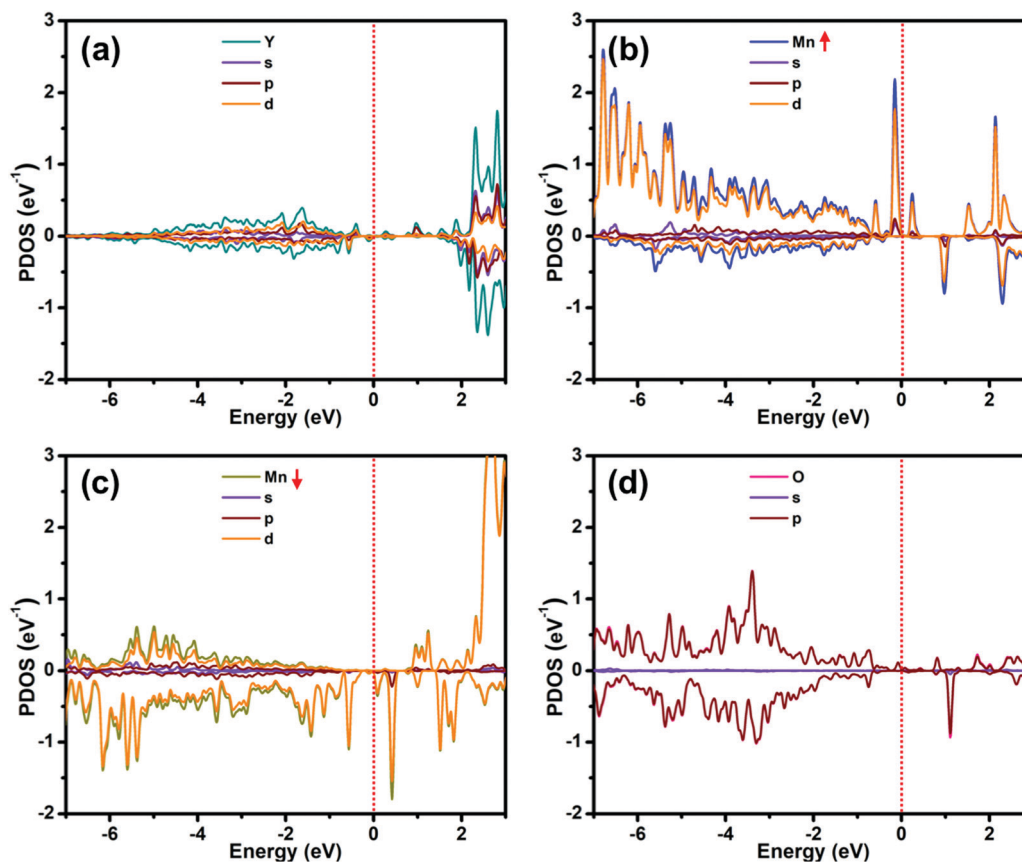


Fig. 6 Orbital-resolved PDOS of pristine  $\text{YMn}_2\text{O}_5(201)$  corresponding to Fig. S3 in the ESI† (a) Y, (b) Mn (majority of spins are up), (c) Mn (majority of spins are down) and (d) O. The red dotted line indicates the Fermi level.

pristine  $\text{YMn}_2\text{O}_5$ , pristine Ag and the  $\text{YMn}_2\text{O}_5$ -Ag composite, respectively (Fig. S4 in the ESI†). From these plots, we see the appearance of an additional shoulder in both the bare  $\text{YMn}_2\text{O}_5$  and  $\text{YMn}_2\text{O}_5$ -Ag spectra, which we speculate to be the signature of the typical out-of-plane ferroelectric polarization in  $\text{YMn}_2\text{O}_5$ . UPS is a surface-sensitive probe and thus any surface-polarized state is expected to be manifested in the collected spectra. It is worth mentioning that ferroelectric polarization can facilitate secondary electron production by making it easier for electrons to escape the sample and reach the photodetector.<sup>63</sup> A suppression of this shoulder peak in the hybrid (Fig. S4c in the ESI†) compared to pristine  $\text{YMn}_2\text{O}_5$  (Fig. S4a in the ESI†) was found, which we believe to be related to the modified surface ferroelectric polarization state resulting from strong interactions between the two systems. Thus, the longest starlight line outside this shoulder region was considered for the determination of the cut-off energy of secondary electrons. The obtained work function values suggest a downward band-bending at the metal-semiconductor interface (Fig. 8). This is indicative of ultrafast hot electron back-scattering following injection into  $\text{YMn}_2\text{O}_5$  from plasmonic Ag, as there is no Schottky barrier to trap them. However, the Schottky barrier for hot holes may trap some injected holes in  $\text{YMn}_2\text{O}_5$ . Thus, the reason for the minor temperature rise observed in Raman thermometry discussed earlier, could be a consequence of the above-mentioned

phenomena coupled with ultrafast cooling of injected hot holes. It is worth mentioning that a possible interfacial ferroelectric polarization will establish an additional interface potential and the equilibration of the work function will modify this polarization over time.<sup>19</sup> The significantly reduced work function of the  $\text{YMn}_2\text{O}_5$ -Ag hybrid compared to those of the pristine metals indicates a much shallower Fermi level of the former. Thus, hot electrons on the surface of the composite are expected to possess higher energy and would be more efficient in photoreduction than hot electrons on the surface of bare Ag. Fig. 8 schematically depicts the possible mechanism of charge carrier dynamics and the Raman surface photocatalytic reduction of 4-NBT to DMAB on pristine Ag and the  $\text{YMn}_2\text{O}_5$ -Ag hybrid.  $\text{YMn}_2\text{O}_5$  has a narrow bandgap of  $\sim 1.5$  eV and photoexcitation of  $\text{YMn}_2\text{O}_5$  generates excitons. Biswas and Jain computed an exciton binding energy of 0.21 eV in the related compound  $\text{YMnO}_3$ .<sup>64</sup> Excitonic electron transfer from  $\text{YMn}_2\text{O}_5$  to Ag is likely to take place according to the HOMO-LUMO analysis discussed earlier. Indeed, plasmonic Ag nanoparticles are likely to increase exciton generation and dissociation in  $\text{YMn}_2\text{O}_5$  through proximity effects, such as local electromagnetic field enhancement and light scattering/trapping.<sup>47,65</sup> PDOS analysis showed an electronic reorganization of states beneficial for enhanced sp-intraband transition needed for hot carrier generation following Landau damping of plasmons.

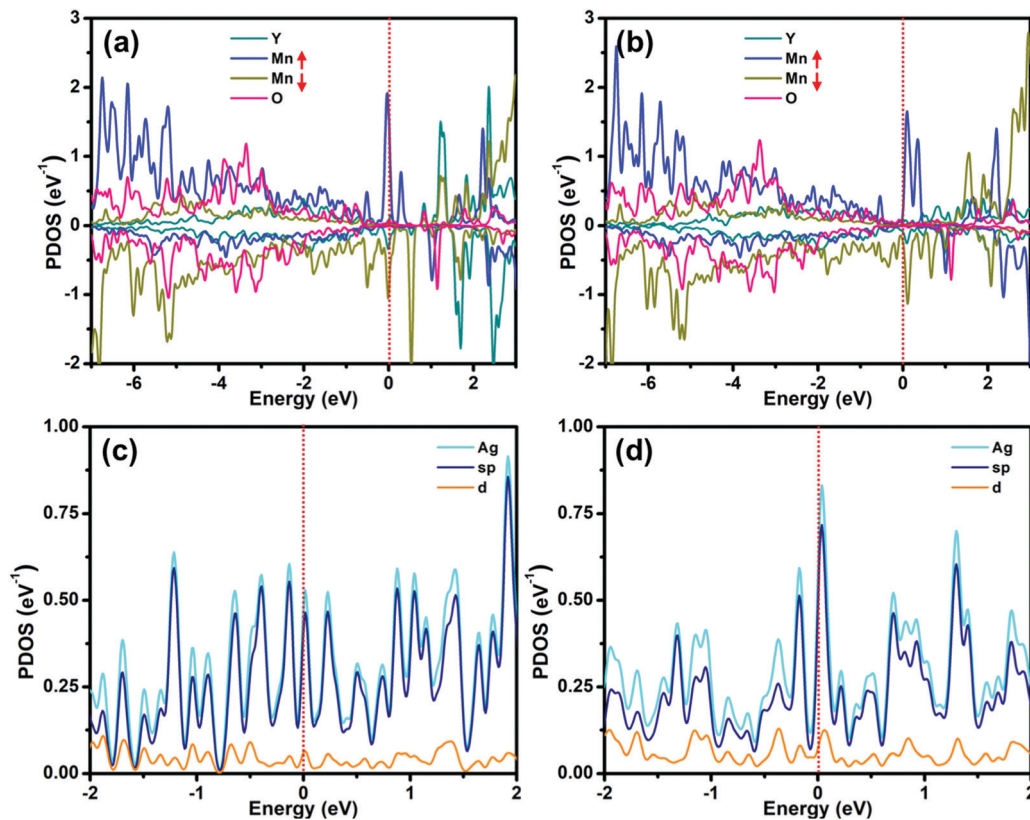
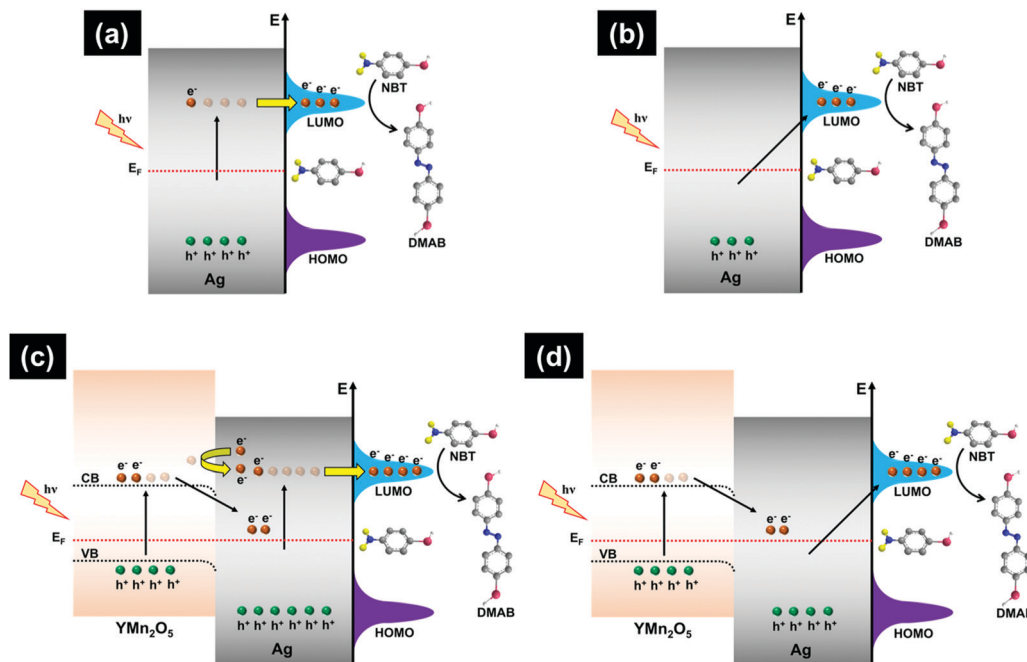


Fig. 7 Projected density of states (PDOS) of Y, Mn, O and Ag atoms of DFT optimized  $\text{YMn}_2\text{O}_5(201)\text{-Ag}(111)$  heterosystems. Y, Mn and O atoms in the (a) far configuration and (b) close configuration. The red arrows indicate two opposite spin dominated Mn atoms. Orbital-resolved PDOS of the Ag atom in the (c) far configuration and (d) close configuration. The red dotted line shows the position of the Fermi level.

Raman thermometry implied no plasmonic hot electron injection into  $\text{YMn}_2\text{O}_5$  from Ag due to the possibility of significant backscattering, resulting from interfacial downward band-bending. Hence, the remarkable photocatalytic performance of the  $\text{YMn}_2\text{O}_5\text{-Ag}$  hybrid in reducing 4-NBT to DMAB compared to stand-alone Ag can be rationalized by the capability of generating a higher population of energetic hot carriers, hot hole transfer from Ag to  $\text{YMn}_2\text{O}_5$ , a possible transfer of photo-excited electrons from  $\text{YMn}_2\text{O}_5$  to Ag and finally a favorable electronic reorganization of the density of states in Ag due to strong interactions with  $\text{YMn}_2\text{O}_5$ .  $\text{YMn}_2\text{O}_5$  exhibits broad absorption over the visible and near-infrared spectral range as shown in Fig. 3b. Therefore, the intriguing possibility exists of pumping the Ag plasmon using the  $\text{YMn}_2\text{O}_5$  absorption, which requires a thorough and separate investigation in a subsequent study. The hot electron-mediated photoreduction of 4-NBT to DMAB can take place either through indirect or direct routes on both bare Ag and the hybrid (Fig. 8). In the indirect mechanism, Landau damping of plasmons generates hot electrons in metallic particles, which enter into the LUMO of the adsorbate molecule (4-NBT), while in the direct mechanism the plasmon relaxation occurs at the metal-adsorbate interfacial hybridized orbitals followed by generation of energetic electrons in the adsorbate molecule's LUMO.<sup>47,48</sup>

### 3. Conclusions

A novel multiferroic-plasmonic hybrid nanowire system was synthesized using a combined hydrothermal and wet-chemical reduction protocol. The TEM and HRTEM images revealed the successful synthesis of  $\text{YMn}_2\text{O}_5$  nanowires. EELS, XRD, DRS and XPS showed strong interaction between  $\text{YMn}_2\text{O}_5$  and Ag. XPS analysis revealed plenty of oxygen vacancies in the nanowires. UPS work function calculation results predicted superior reducing power of plasmonic hot electrons generated on the composite's surface. The hybrid system demonstrated superior performance in photoreducing 4-NBT into DMAB compared to stand-alone Ag. The higher photocatalytic performance was also attributable to reduced hot carrier pair recombination due to hot hole injection from Ag into  $\text{YMn}_2\text{O}_5$ . The molecular orbital plots calculated from DFT were supportive of hole injection from  $\text{YMn}_2\text{O}_5$  to Ag. DFT results indicated two additional noteworthy features – the first being an electronic contribution to the ferroelectric polarization in  $\text{YMn}_2\text{O}_5$  over and above any ionic contributions, and the second being enhanced hot carrier generation in Ag- $\text{YMn}_2\text{O}_5$  hybrids. PDOS analysis revealed a redistribution of the electronic density of states of Ag atoms upon interaction with  $\text{YMn}_2\text{O}_5$ , supportive of a more favourable sp-intraband transition, involved in plasmon relaxation-mediated hot carrier generation in silver. Stokes



**Fig. 8** Mechanisms for surface photocatalytic reduction of 4-NBT to DMAB on pristine Ag and  $\text{YMn}_2\text{O}_5$ -Ag hybrid. (a) Indirect hot electron transfer from pristine Ag into the LUMO of 4-NBT. (b) Direct hot electron transfer from pristine Ag into the LUMO of 4-NBT. (c) Indirect hot electron transfer from the  $\text{YMn}_2\text{O}_5$ -Ag hybrid into the LUMO of 4-NBT. (d) Direct hot electron transfer from the  $\text{YMn}_2\text{O}_5$ -Ag hybrid into the LUMO of 4-NBT. In the molecular structures - red, grey, blue, yellow and silver colours represent O, C, N, S and H atoms, respectively.

anti-Stokes Raman thermometry data coupled with DFT calculations provided useful information in the elucidation of charge carrier and plasmon relaxation dynamics. This study shows the potential of coupled multiferroic-plasmonic systems in the solar energy harvesting arena.

## Conflicts of interest

There are no conflicts to declare.

## Acknowledgements

The authors acknowledge the National Research Council Canada (NRC) for primary funding support. The authors acknowledge direct and indirect support from the Natural Sciences and Engineering Research Council of Canada (NSERC) and University of Alberta Future Energy Systems (FES) CFREF. Narendra Chaulagain's assistance in revising the manuscript is acknowledged.

## References

- N. A. Spaldin and R. Ramesh, Advances in magnetoelectric multiferroics, *Nat. Mater.*, 2019, **18**(3), 203–212.
- S. W. Cheong and M. Mostovoy, Multiferroics: a magnetic twist for ferroelectricity, *Nat. Mater.*, 2007, **6**(1), 13–20.
- N. A. Spaldin, S.-W. Cheong and R. Ramesh, Multiferroics: Past, present, and future, *Phys. Today*, 2010, **63**(10), 38–43.
- D. P. Kozlenko, N. T. Dang, S. E. Kichanov, E. V. Lukin, A. M. Pashayev, A. I. Mammadov, S. H. Jabarov, L. S. Dubrovinsky, H. P. Liermann, W. Morgenroth, R. Z. Mehdiyeva, V. G. Smotrakov and B. N. Savenko, Competing magnetic and structural states in multiferroic  $\text{YMn}_2\text{O}_5$  at high pressure, *Phys. Rev. B: Condens. Matter Mater. Phys.*, 2015, **92**(13), 134409.
- X. Tang and L. Kou, Two-Dimensional Ferroics and Multiferroics: Platforms for New Physics and Applications, *J. Phys. Chem. Lett.*, 2019, **10**(21), 6634–6649.
- M. Fiebig, T. Lottermoser, D. Meier and M. Trassin, The evolution of multiferroics, *Nat. Rev. Mater.*, 2016, **1**(8), 16046.
- N. A. Spaldin, Multiferroics beyond electric-field control of magnetism, *Proc. R. Soc. A*, 2020, **476**(2233), 20190542.
- G. Catalan and J. F. Scott, Physics and Applications of Bismuth Ferrite, *Adv. Mater.*, 2009, **21**(24), 2463–2485.
- S. H. Chu, D. J. Singh, J. Wang, E. P. Li and K. P. Ong, High optical performance and practicality of active plasmonic devices based on rhombohedral  $\text{BiFeO}_3$ , *Laser Photonics Rev.*, 2012, **6**(5), 684–689.
- D. Cao, Z. Wang, Nasori, L. Wen, Y. Mi and Y. Lei, Switchable charge-transfer in the photoelectrochemical energy-conversion process of ferroelectric  $\text{BiFeO}_3$  photoelectrodes, *Angew. Chem., Int. Ed.*, 2014, **53**(41), 11027–11031.
- S. Irfan, Z. Zhuanghao, F. Li, Y.-X. Chen, G.-X. Liang, J.-T. Luo and F. Ping, Critical review: Bismuth ferrite as an emerging visible light active nanostructured photocatalyst, *J. Mater. Res. Technol.*, 2019, **8**(6), 6375–6389.
- S. Dong, J.-M. Liu, S.-W. Cheong and Z. Ren, Multiferroic materials and magnetoelectric physics: symmetry, entanglement, excitation, and topology, *Adv. Phys.*, 2015, **64**(5-6), 519–626.

- 13 T. Zhang, H. Li, Z. Yang, F. Cao, L. Li, H. Chen, H. Liu, K. Xiong, J. Wu, Z. Hong and W. Wang, Electrospun  $\text{YMn}_2\text{O}_5$  nanofibers: A highly catalytic activity for NO oxidation, *Appl. Catal., B*, 2019, **247**, 133–141.
- 14 T. Zhang, X. Lang, A. Dong, X. Wan, S. Gao, L. Wang, L. Wang and W. Wang, Difference of Oxidation Mechanism between Light C3–C4 Alkane and Alkene over Mullite  $\text{YMn}_2\text{O}_5$  Oxides' Catalyst, *ACS Catal.*, 2020, **10**(13), 7269–7282.
- 15 H. Yang, S. F. Wang, T. Xian, Z. Q. Wei and W. J. Feng, Fabrication and photocatalytic activity of  $\text{YMn}_2\text{O}_5$  nanoparticles, *Mater. Lett.*, 2011, **65**(5), 884–886.
- 16 R. Jiang, B. Li, C. Fang and J. Wang, Metal/Semiconductor hybrid nanostructures for plasmon-enhanced applications, *Adv. Mater.*, 2014, **26**(31), 5274–5309.
- 17 E. Cortes, Activating plasmonic chemistry, *Science*, 2018, **362**(6410), 28–29.
- 18 S. Zeng, E. Vahidzadeh, C. G. VanEssen, P. Kar, R. Kisslinger, A. Goswami, Y. Zhang, N. Mandi, S. Riddell, A. E. Kobryn, S. Gusarov, P. Kumar and K. Shankar, Optical control of selectivity of high rate  $\text{CO}_2$  photoreduction via interband hot electron Z-scheme reaction pathways in Au-TiO<sub>2</sub> plasmonic photonic crystal photocatalyst, *Appl. Catal., B*, 2020, 267.
- 19 V. Kumar, S. C. O'Donnell, D. L. Sang, P. A. Maggard and G. Wang, Harnessing Plasmon-Induced Hot Carriers at the Interfaces With Ferroelectrics, *Front. Chem.*, 2019, **7**, 299.
- 20 N. Ortiz, B. Zoellner, V. Kumar, T. Janelli, S. Tang, P. A. Maggard and G. Wang, Composite Ferroelectric and Plasmonic Particles for Hot Charge Separation and Photocatalytic Hydrogen Gas Production, *ACS Appl. Energy Mater.*, 2018, **1**(9), 4606–4616.
- 21 V. Kumar, S. O'Donnell, B. Zoellner, J. Martinez, G. Wang and P. A. Maggard, Interfacing Plasmonic Nanoparticles with Ferroelectrics for Hot-Carrier-Driven Photocatalysis: Impact of Schottky Barrier Height, *ACS Appl. Energy Mater.*, 2019, **2**(10), 7690–7699.
- 22 Z. Wang, D. Cao, L. Wen, R. Xu, M. Obergfell, Y. Mi, Z. Zhan, N. Nasori, J. Demsar and Y. Lei, Manipulation of charge transfer and transport in plasmonic-ferroelectric hybrids for photoelectrochemical applications, *Nat. Commun.*, 2016, **7**, 10348.
- 23 W. Huang, C. Harnagea, D. Benetti, M. Chaker, F. Rosei and R. Nechache, Multiferroic  $\text{Bi}_2\text{FeCrO}_6$  based p–i–n heterojunction photovoltaic devices, *J. Mater. Chem. A*, 2017, **5**(21), 10355–10364.
- 24 W. Huang, J. Chakraborty, C. Harnagea, D. Gedamu, I. Ka, M. Chaker, F. Rosei and R. Nechache, Highly Sensitive Switchable Heterojunction Photodiode Based on Epitaxial  $\text{Bi}_2\text{FeCrO}_6$  Multiferroic Thin Films, *ACS Appl. Mater. Interfaces*, 2018, **10**(15), 12790–12797.
- 25 A. Gomez-Tornero, C. Tserkezis, L. Mateos, L. E. Bausa and M. O. Ramirez, 2D Arrays of Hexagonal Plasmonic Necklaces for Enhanced Second Harmonic Generation, *Adv. Mater.*, 2017, **29**(15), 1605267.
- 26 C. Lu, X. Hu, S. Yue, Y. Fu, H. Yang and Q. Gong, Ferroelectric Hybrid Plasmonic Waveguide for All-Optical Logic Gate Applications, *Plasmonics*, 2012, **8**(2), 749–754.
- 27 M. O. Ramirez, P. Molina, A. Gomez-Tornero, D. Hernandez-Pinilla, L. Sanchez-Garcia, S. Carretero-Palacios and L. E. Bausa, Hybrid Plasmonic-Ferroelectric Architectures for Lasing and SHG Processes at the Nanoscale, *Adv. Mater.*, 2019, **31**(35), e1901428.
- 28 K. Wang, X. Xu, L. Lu, H. Wang, Y. Li, Y. Wu, J. Miao, J. Z. Zhang and Y. Jiang, Enhanced and Facet-specific Electrocatalytic Properties of  $\text{Ag}/\text{Bi}_2\text{Fe}_4\text{O}_9$  Composite Nanoparticles, *ACS Appl. Mater. Interfaces*, 2018, **10**(15), 12698–12707.
- 29 X. Cheng, H. Shen, W. Dong, F. Zheng, L. Fang, X. Su and M. Shen, Nano-Au and Ferroelectric Polarization Mediated Si/ITO/ $\text{BiFeO}_3$  Tandem Photocathode for Efficient  $\text{H}_2$  Production, *Adv. Mater. Interfaces*, 2016, **3**(19), 1600485.
- 30 S. Mohan, B. Subramanian and G. Sarveswaran, A prototypical development of plasmonic multiferroic bismuth ferrite particulate and fiber nanostructures and their remarkable photocatalytic activity under sunlight, *J. Mater. Chem. C*, 2014, **2**(33), 6835–6842.
- 31 X. Xu, K. Seal, X. Xu, I. Ivanov, C. H. Hsueh, N. A. Hatab, L. Yin, X. Zhang, Z. Cheng, B. Gu, Z. Zhang and J. Shen, High tunability of the surface-enhanced Raman scattering response with a metal-multiferroic composite, *Nano Lett.*, 2011, **11**(3), 1265–1269.
- 32 C. H. Vivas and C. Vargas-Hernández, Optical reflectivity and magnetoelectric effects on resonant plasmon modes in composite metal-multiferroic systems, *Opt. Commun.*, 2013, **311**, 354–358.
- 33 E. Vahidzadeh, S. Zeng, K. M. Alam, P. Kumar, S. Riddell, N. Chaulagain, S. Gusarov, A. E. Kobryn and K. Shankar, Harvesting Hot Holes in Plasmon-Coupled Ultrathin Photoanodes for High-Performance Photoelectrochemical Water Splitting, *ACS Appl. Mater. Interfaces*, 2021, **13**(36), 42741–42752.
- 34 G. Tagliabue, J. S. DuChene, M. Abdellah, A. Habib, D. J. Gosztola, Y. Hattori, W. H. Cheng, K. Zheng, S. E. Canton, R. Sundararaman, J. Sa and H. A. Atwater, Ultrafast hot-hole injection modifies hot-electron dynamics in Au/p-GaN heterostructures, *Nat. Mater.*, 2020, **19**(12), 1312–1318.
- 35 G. Tagliabue, J. S. DuChene, A. Habib, R. Sundararaman and H. A. Atwater, Hot-Hole versus Hot-Electron Transport at Cu/GaN Heterojunction Interfaces, *ACS Nano*, 2020, **14**(5), 5788–5797.
- 36 J. Shi, J. Wang, H. He, Y. Lu and Z. Shi, Rodlike  $\text{YMn}_2\text{O}_5$  Powders Derived from Hydrothermal Process Using Oxygen as Oxidant, *Materials*, 2020, **13**(3), 805.
- 37 Y. Mei and S. Wu, Morphology control of  $\text{YMn}_2\text{O}_5$  nanocrystals by hydrothermal synthesis and their magnetic properties, *RSC Adv.*, 2013, **3**(29), 11888–11894.
- 38 L. L. Li, S. Y. Wu and X. M. Chen, Multiferroic  $\text{YMn}_2\text{O}_5$  fine powders derived from hydrothermal process, *J. Mater. Sci.: Mater. Electron.*, 2009, **20**(12), 1159–1163.
- 39 M. L. Debasu, J. C. Riedl, J. Rocha and L. D. Carlos, The role of  $\text{Li}^{(+)}$  in the upconversion emission enhancement of  $(\text{YbEr})_2\text{O}_3$  nanoparticles, *Nanoscale*, 2018, **10**(33), 15799–15808.

- 40 H. Xia, C. Hong, X. Shi, B. Li, G. Yuan, Q. Yao and J. Xie, Hierarchical heterostructures of Ag nanoparticles decorated MnO<sub>2</sub> nanowires as promising electrodes for supercapacitors, *J. Mater. Chem. A*, 2015, **3**(3), 1216–1221.
- 41 J. Gazquez, A. Carretero-Genevri, M. Gich, N. Mestres and M. Varela, Electronic and magnetic structure of LaSr<sub>2</sub>x<sub>4</sub> manganese oxide molecular sieve nanowires, *Microsc. Microanal.*, 2014, **20**(3), 760–766.
- 42 Z. Chen, R.-J. Xiao, C. Ma, Y.-B. Qin, H.-L. Shi, Z.-W. Wang, Y.-J. Song, Z. Wang, H.-F. Tian, H.-X. Yang and J.-Q. Li, Electronic structure of YMn<sub>2</sub>O<sub>5</sub> studied by EELS and first-principles calculations, *Front. Phys.*, 2011, **7**(4), 429–434.
- 43 A. Travlos, N. Boukos, G. Apostolopoulos and A. Dimoulas, Oxygen vacancy ordering in epitaxial layers of yttrium oxide on Si (001), *Appl. Phys. Lett.*, 2003, **82**(23), 4053–4055.
- 44 W. Wu, M. Wu, Z. Sun, G. Li, Y. Ma, X. Liu, X. Wang and X. Chen, Morphology controllable synthesis of silver nanoparticles: Optical properties study and SERS application, *J. Alloys Compd.*, 2013, **579**, 117–123.
- 45 R. C. Maher, C. M. Galloway, E. C. Le Ru, L. F. Cohen and P. G. Etchegoin, Vibrational pumping in surface enhanced Raman scattering (SERS), *Chem. Soc. Rev.*, 2008, **37**(5), 965–979.
- 46 D. Tuschel, Raman Thermometry, *Spectroscopy*, 2016, **31**(12), 8–13.
- 47 Y. Zhang, S. He, W. Guo, Y. Hu, J. Huang, J. R. Mulcahy and W. D. Wei, Surface-Plasmon-Driven Hot Electron Photochemistry, *Chem. Rev.*, 2018, **118**(6), 2927–2954.
- 48 A. P. Manuel, A. Kirkey, N. Mahdi and K. Shankar, Plexcitonics - fundamental principles and optoelectronic applications, *J. Mater. Chem. C*, 2019, **7**(7), 1821–1853.
- 49 A. P. Manuel and K. Shankar, Hot Electrons in TiO<sub>2</sub>-Noble Metal Nano-Heterojunctions: Fundamental Science and Applications in Photocatalysis, *Nanomaterials*, 2021, **11**(5), 1249.
- 50 C. Boerigter, R. Campana, M. Morabito and S. Linic, Evidence and implications of direct charge excitation as the dominant mechanism in plasmon-mediated photocatalysis, *Nat. Commun.*, 2016, **7**, 10545.
- 51 X. C. Ma, Y. Dai, L. Yu and B. B. Huang, Energy transfer in plasmonic photocatalytic composites, *Light: Sci. Appl.*, 2016, **5**(2), e16017.
- 52 B. Dong, Y. Fang, X. Chen, H. Xu and M. Sun, Substrate-, wavelength-, and time-dependent plasmon-assisted surface catalysis reaction of 4-nitrobenzenethiol dimerizing to p,p'-dimercaptoazobenzene on Au, Ag, and Cu films, *Langmuir*, 2011, **27**(17), 10677–10682.
- 53 Q. Ding, R. Li, M. Chen and M. Sun, Ag nanoparticles-TiO<sub>2</sub> film hybrid for plasmon-exciton co-driven surface catalytic reactions, *Appl. Mater. Today*, 2017, **9**, 251–258.
- 54 V. Canpean, M. Iosin and S. Astilean, Disentangling SERS signals from two molecular species: A new evidence for the production of p,p'-dimercaptoazobenzene by catalytic coupling reaction of p-aminothiophenol on metallic nanostructures, *Chem. Phys. Lett.*, 2010, **500**(4-6), 277–282.
- 55 H.-Y. Wu, Y.-H. Lai, M.-S. Hsieh, S.-D. Lin, Y.-C. Li and T.-W. Lin, Highly Intensified Surface Enhanced Raman Scattering through the Formation of p,p'-Dimercaptoazobenzene on Ag Nanoparticles/Graphene Oxide Nanocomposites, *Adv. Mater. Interfaces*, 2014, **1**(8), 1400119.
- 56 M. Savarese, E. Bremond, I. Ciofini and C. Adamo, Electron Spin Densities and Density Functional Approximations: Open-Shell Polycyclic Aromatic Hydrocarbons as Case Study, *J. Chem. Theory Comput.*, 2020, **16**(6), 3567–3577.
- 57 S. Partzsch, S. B. Wilkins, E. Schierle, J. E. Hamann-Borrero, H. Wadati, V. Soltwisch, J. P. Hill, E. Weschke, D. Souptel, B. Büchner and J. Geck, Resonant soft X-ray scattering studies of multiferroic YMn<sub>2</sub>O<sub>5</sub>, *Eur. Phys. J.: Spec. Top.*, 2012, **208**(1), 133–139.
- 58 S. Partzsch, S. B. Wilkins, J. P. Hill, E. Schierle, E. Weschke, D. Souptel, B. Buchner and J. Geck, Observation of electronic ferroelectric polarization in multiferroic YMn<sub>2</sub>O<sub>5</sub>, *Phys. Rev. Lett.*, 2011, **107**(5), 057201.
- 59 R. A. de Souza, U. Staub, V. Scagnoli, M. Garganourakis, Y. Bodenthin, S. W. Huang, M. García-Fernández, S. Ji, S. H. Lee, S. Park and S. W. Cheong, Magnetic structure and electric field effects in multiferroic YMn<sub>2</sub>O<sub>5</sub>, *Phys. Rev. B: Condens. Matter Mater. Phys.*, 2011, **84**(10), 104416.
- 60 K.-Q. Lin, J. Yi, S. Hu, J.-J. Sun, J.-T. Zheng, X. Wang and B. Ren, Intraband Hot-Electron Photoluminescence from Single Silver Nanorods, *ACS Photonics*, 2016, **3**(7), 1248–1255.
- 61 O. A. Douglas-Gallardo, M. Berdakin, T. Frauenheim and C. G. Sanchez, Plasmon-induced hot-carrier generation differences in gold and silver nanoclusters, *Nanoscale*, 2019, **11**(17), 8604–8615.
- 62 A. M. Brown, R. Sundararaman, P. Narang, W. A. Goddard and H. A. Atwater, Nonradiative Plasmon Decay and Hot Carrier Dynamics: Effects of Phonons, Surfaces, and Geometry, *ACS Nano*, 2016, **10**(1), 957–966.
- 63 N. G. Apostol, L. E. Stoflea, G. A. Lungu, C. Chirila, L. Trupina, R. F. Negrea, C. Ghica, L. Pintilie and C. M. Teodorescu, Charge transfer and band bending at Au/Pb(Zr<sub>0.2</sub>Ti<sub>0.8</sub>)O<sub>3</sub> interfaces investigated by photoelectron spectroscopy, *Appl. Surf. Sci.*, 2013, **273**, 415–425.
- 64 T. Biswas and M. Jain, Quasiparticle band structure and optical properties of hexagonal-YMnO<sub>3</sub>, *J. Appl. Phys.*, 2016, **120**(15), 155102.
- 65 L. Mascaretti, A. Dutta, S. Kment, V. M. Shalaev, A. Boltasseva, R. Zboril and A. Naldoni, Plasmon-Enhanced Photoelectrochemical Water Splitting for Efficient Renewable Energy Storage, *Adv. Mater.*, 2019, **31**(31), e1805513.